

Shot-to-shot acquisition ultrafast electron diffraction

Rémi Claude,¹ Michele Puppin,¹ Bruce Weaver,¹ Paolo Usai,¹ Thomas La Grange,¹ and Fabrizio Carbone¹

*Laboratory of Ultrafast Microscopy and Electron scattering,
Ecole Polytechnique Fédérale de Lausanne*

(*Electronic mail: fabrizio.carbone@epfl.ch)

(Dated: 5 February 2025)

We demonstrate a novel shot-to-shot acquisition method for optical pump - keV electron energy probe in ultrafast scattering experiments. We integrate a phase-locked acquisition scheme at a repetition rate of 20kHz in a conventional ultrafast electron diffraction (UED) setup. We proceed to a full characterization of the noise level in different configurations and of the temporal resolution as a function of electron flux. The shot-to-shot acquisition improves the signal-to-noise ratio (SNR) by one order of magnitude in a low perturbation regime.

I. INTRODUCTION

Ultrafast electron diffraction, microscopy, and energy loss spectroscopy are widely used to investigate the properties of materials out-of-equilibrium using pump-probe methods¹. Transient signals recorded by these techniques correspond to a variation in the number of scattered electrons at specific positions in the momentum, real, or energy space, which enables studies in the temporal domain of lattice dynamics^{2,3}, magnetic ordering⁴⁻⁶, plasmon dynamics⁷, charge density waves coherent response and melting⁸, and to resolve changes in the phonon population with momentum resolution⁹⁻¹¹. The amplitude of transient signals increases with the photoexcitation energy density and is typically in the order of percent for light excitation in the range of mJ/cm^2 . Advanced material science rely on broken-symmetry ground states where a delicate microscopic balance of electron, spin, lattice and orbital degree of freedom is attained. While elastically scattered electrons provide measurements of lattice order, inelastically scattered electrons contain crucial information on the momentum-dependent interaction between collective modes¹². For instance, phonon populations alter thermal diffuse scattering, which has a typically total cross-section of 10^{-4} . Other quasiparticles such as magnons are also present in the diffuse inelastic scattering but represent only 10^{-6} of the total electron flux¹³. Time-resolved measurements of such inelastic signals present a significant challenge for current experimental setups, which must improve detection sensitivity to capture small photo-induced variations, particularly in weak perturbation regimes that maintain the integrity of the ground state.

To improve the signal-to-noise ratio (SNR), a first possibility is to develop a brighter electron source ($> 10^5$ electrons/pulse). However, this approach introduces space-charge-induced temporal broadening of the electron pulse, which significantly degrades the time resolution^{14,15}. Temporal compression of the electron bunch can be achieved using a synchronized radio frequency cavity^{16,17} or a terahertz (THz) optical pulse¹⁸. Nevertheless, special care must be taken to avoid jitter and long-term drifts¹⁹. A second approach is to minimize the noise of the electron source, while working at low electron flux ($< 10^4$ electron/pulse). To mitigate space charge broadening, the electron source is placed as close as possible to the sample²⁰. Combined with a high repetition rate laser source and fast acquisition system^{21,22}, the SNR is increased while maintaining good beam coherence. A possible limitation of this method is the sample re-equilibration time, which can become greater than the inter-pulse separation ($< 1\mu\text{s}$). In this work, we describe an ultrafast electron scattering apparatus based on a source with a pulse repetition rate of 20 kHz operating

at a low flux of a thousand electrons per pulse. In this limit, the quality of the acquisition system is essential to improve the SNR. We employ a direct electron detector²³, which records high SNR electron diffraction patterns²⁴ thanks to a combination of high detective quantum efficiency (DQE) (0.9 for direct detection, as compared to 0.2 for a typical CCD)²⁵ and low acquisition noise. Another advantage of such a direct detection system is its capability to acquire data at a high rate, synchronized with the laser repetition rate²⁶. This enables the collection of pump-probe data by chopping the pump pulse train at 10 kHz and normalizing the data using unpumped acquisition frames. This method, well-established in ultrafast optical spectroscopy due to the availability of fast light detectors, is widely used to achieve shot-noise-limited data²⁷. For electron scattering experiments, where the number of events per pixel per laser pulse is relatively low, this approach is feasible due to the detector's negligibly low dark count rate. We demonstrate pump-probe data with a noise level reaching 10^{-4} in a few hours of acquisition time, with a time resolution in the sub-picosecond range.

The paper is organized as follows. In section II, we describe the setup, the acquisition system, and the working principles of the synchronization to achieve the shot-to-shot acquisition. Section III presents the characterization of the noise level and the time resolution. In section IV, we will present UED data acquired in a realistic scenario by photo-exciting graphite samples with an 800 nm pump.

II. DESIGN OF THE SHOT-TO-SHOT UED

A. Optical setup and electron diffraction beamline

The ultrafast electron diffraction (UED) setup and the data acquisition scheme are schematized in Fig. 1. The current setup is a modification of the setup detailed in Ref.¹⁶. A cryogenically cooled Ti:Sapphire laser²⁸ provides 50 fs pulses at a central wavelength of 780 nm at a repetition rate of 20 kHz with an output power higher than 10 W (pulse energy > 0.5 mJ). To avoid long-term drifts, the laser beam pointing is stabilized by a home-built stabilization system based on a pair of piezoelectric-actuated mirrors and CMOS cameras. The beam is divided into two arms with a beam splitter (BS1).

The pump beam goes through a mechanical delay line, to vary the delay between the probe pulse and the pump pulse. Then, is passed through a mechanical chopper, synchronized with the laser

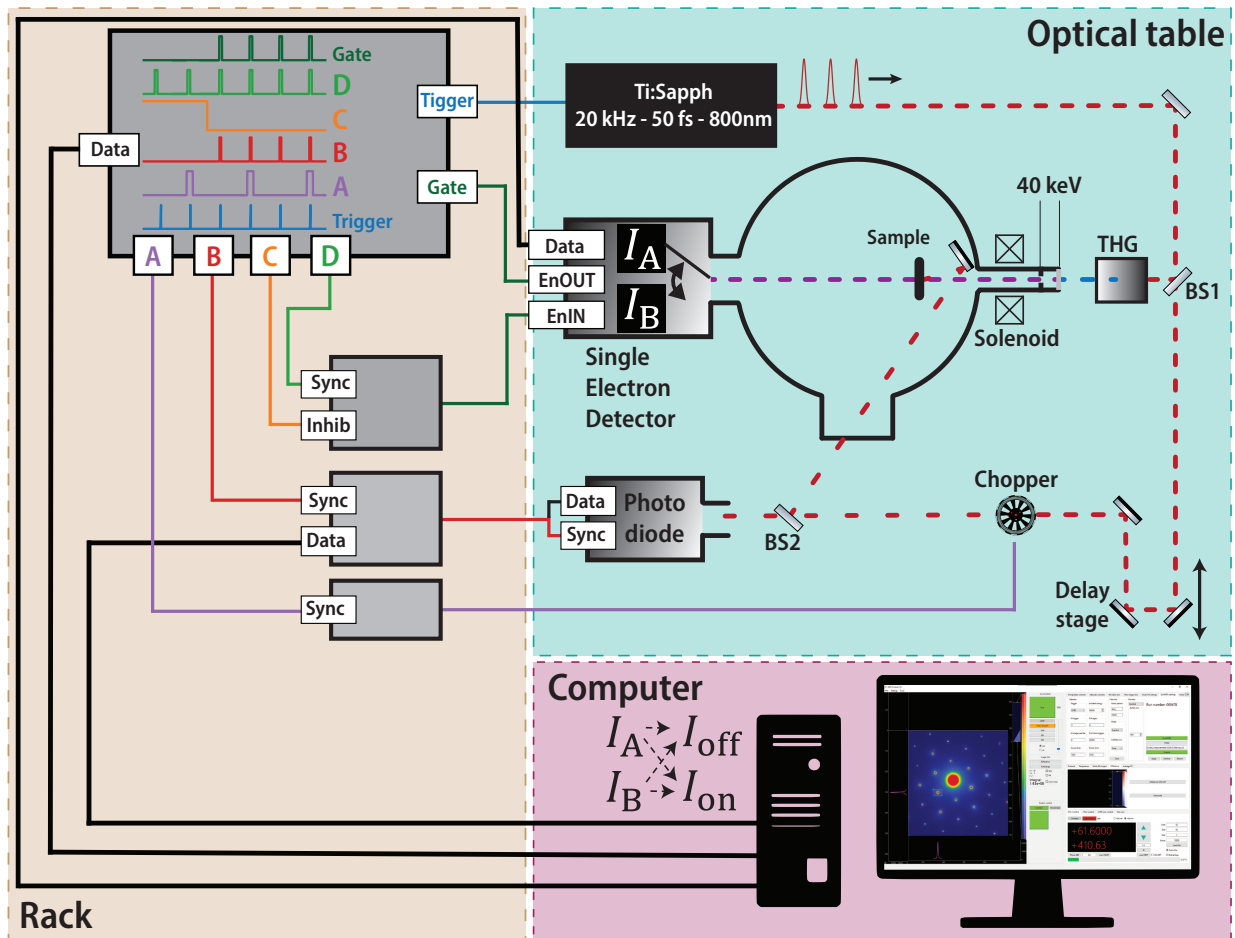


FIG. 1. Scheme of the UED setup in EPFL composed of the optical table, the rack, and the computer. The optical table supports the pulsed laser, the optical beam path divided into pump and probe arms, the vacuum sample chamber, the electron and photodiode detector. The rack accommodates the synchronization system which is phase-locked with the laser source at 20 kHz. The data gathered by the electron and photodiode detector are sent the computer to be sorted between pumped and unpumped diffraction patterns.

source to halve the pulse repetition rate to 10 kHz. The last mirror (BS2) sends the pump into the chamber and is used to find spatial overlap between the pump beam and the electron probe. BS2 also acts as a beam splitter, transmitting a small fraction of the pump towards a photodiode.

In the probe arm, third harmonic generation (THG) is used to generate a UV light beam (260 nm) which back-illuminates a silver-coated sapphire photo-cathode. The UV probe pulse energy exceeds the work function of the silver ($P_{UV} = 4.76 \text{ eV} > W_{Ag} = 4.26 \text{ eV}$), thus generating a pulse of electrons by single-photon photoemission, with a measured quantum efficiency of 10^{-8} electron/photon (see Appendix A). These pulses are then accelerated up to 40 keV over a distance

of 3 mm corresponding to an accelerating electric field of 13.3 MV/m. The electron beam is focused by a homemade magnetic lens consisting of around 3000 windings, each of them carrying a current of 0.62 A.

After 150 mm of propagation length, the electron pulses reach the sample holder position with sub-ps pulse duration, depending on the electron flux, as described in Sec III C. In transmission geometry, a copper sample holder hosts five standard 3 mm TEM grids. The holder is mounted on a 4-axis open-cycle cryo-manipulator that can achieve a temperature of 4.2K with liquid helium cooling. The UED setup can also work in reflection geometry to probe the surface lattice dynamics with five axes of freedom using another sample holder²⁹.

The vacuum chamber has a base pressure of 10^{-8} mbar and accommodates a mirror that reflects the pump beams onto the sample with an angle of a few degrees off from the electron beam.

The electron beam travels a distance of 491 mm after the sample position. At this distance and with a chip detection size of 38.4×38.4 mm², a reciprocal space area of 16×16 Å⁻² is covered at 40 keV.

B. High speed lock-in direct electron detection

The direct electron sensor is Si-based with 512×512 hybrid-pixels with a DQE of 0.9 at 100 keV and can acquire electrons from 30 keV to 200 keV, without readout noise. However, after an electron collides with a pixel, it remains triggered for 50 ns, thus the detector cannot acquire more than one electron per pulse per pixel, which reduces the QDE for high pulsed electron flux as explained in Appendix B. The fast electronics allow an acquisition rate of 2250 frames per second and up to 18000 frames per second for a reduced region of interest (ROI). Each pixel has two 16-bit counter chips to reach a bit depth of 32-bit. Importantly for this work, it is also possible to switch between these 16-bit counters within 200 ns, sorting electron events independently in each of the two counters. The acquisition window is externally controlled by a time to live signal at a rate of 20 kHz, locked to the laser repetition rate. We note that rates exceeding 1 MHz are in principle possible by this method. After a given number of acquisition windows (typically $4 \cdot 10^4 \equiv 2$ s), the total number of counts acquired for the two counters of each pixel is transferred as two full-frame images, labeled I_A and I_B in the figure. In this way, the effective repetition rate of the acquisition is greatly improved while minimizing the data transfer.

We use this detector feature to acquire ultrafast electron diffraction by chopping the pump pulses

at half the laser repetition rate (10 kHz). The two output images correspond to the excited, I_{on} , and nonexcited, I_{off} , diffraction patterns of the studied sample. Due to the high shot-to-shot correlation of the laser source, this reduces considerably the noise in the pump-probe signal, as will be discussed in Sec. III. We now describe the synchronization system in greater detail.

C. Synchronization system

To capture the single shots, we synchronize the detection with the time of arrival of the electrons to the laser source repetition.

As schematized in the left panel of Fig. 1, a homemade delay generator constantly receives the 20 kHz laser signal from the laser source. This trigger is relayed by a homemade delay generator into four independently-delayed channels (A-D). Channel A is frequency-divided to 10 kHz and transmitted to the chopper controller. Channel B triggers a fast photodiode digitizer³⁰. This signal on this channel is gated by the main detector (EnOUT) which is a replica of the one received (EnIN). This way, the Quadro detector operates as master and the photo-diode as slave, ensuring that the same pulses originating from the laser are detected. The electron detector acquisition window is controlled by channel D, with a 20 kHz repetition rate with a window of 25 μs . The acquisition window from channel D is inhibited by channel C, acting like a switch controlled by the main computer to start the acquisition without cutting off pulses. This synchronization system allows a robust acquisition of every single electron bunch at 20 kHz, but can easily be adjusted to other repetition rates although the chopping mechanism would be different for higher frequencies. From the main computer, the number of exposition windows, n , as well as other settings of the detector can be monitored.

The main computer accesses the two 2D datasets acquired by the electron detector, I_A and I_B that can be sorted into I_{on} and I_{off} , thanks to the photodiode. The GUI can live display these data and the difference between $I_{\text{on}} - I_{\text{off}}$ allowing for an accurate time and spatial overlap.

III. CHARACTERIZATION

Given the low shot-to-shot fluctuation of the laser source, this acquisition method can greatly improve the SNR of ultrafast experiments. We characterize this enhancement by disentangling the noise sources for conventional and shot-to-shot acquisition techniques with and without the

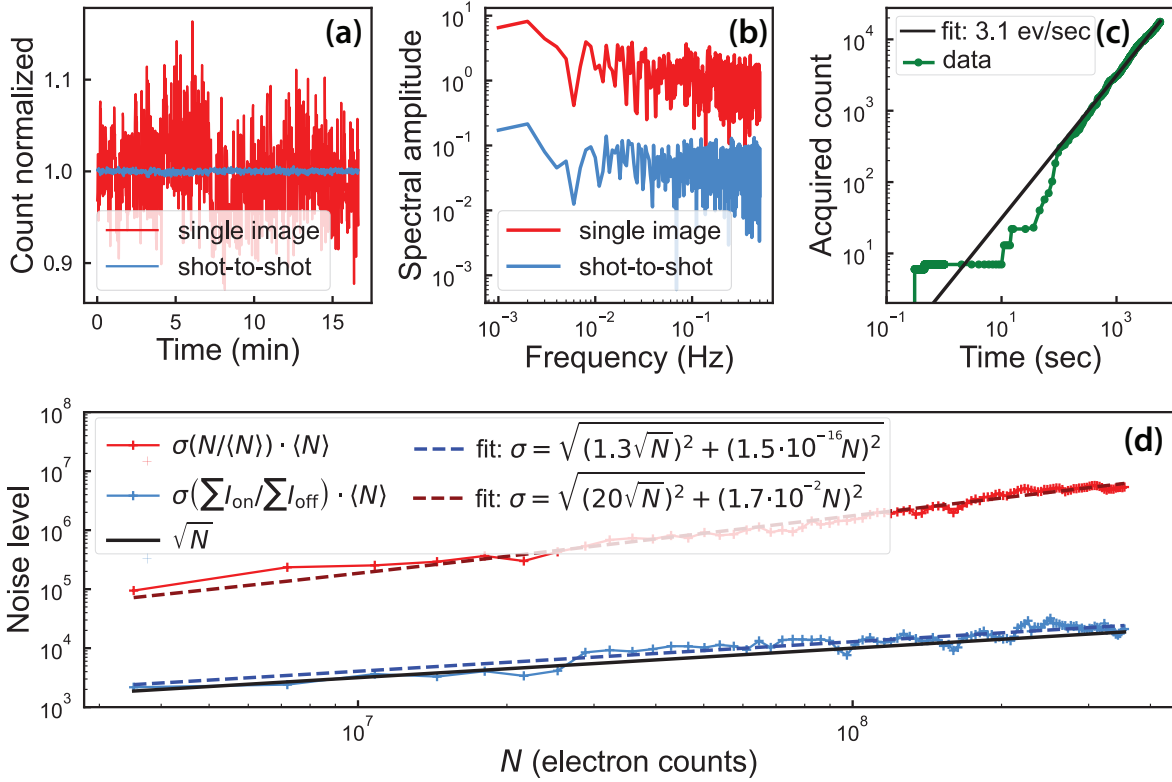


FIG. 2. a) Fluctuation of the electron diffraction pattern of Graphite sample in the absence of a pump as a function of time for an exposure time of one second, with a flux of $3.6 \cdot 10^6$ electrons/sec. b) Spectral amplitude of the electron fluctuation as a function of the frequency, which corresponds to the Fourier transform of Fig 2a. c) Acquired count without electron beam as a function of the integration time due to cosmic ray having a flux of 3.1 events/sec from a linear fit. d) Variation of the noise level as a function of the cumulative signal N for different configurations. The experimental curve is fitted with equation 2.

photoexcitation pulse. We also investigate the electron pulse duration of our system as a function of the flux to find the optimal compromise between electron flux and time resolution.

A. Noise level without pump

We acquired a series of diffraction patterns on a 50 nm thick Graphite single crystal. Data were recorded as a function of pump-probe delay time with the shot-to-shot acquisition system. For each acquisition window (i), two diffraction patterns corresponding to I_{on} and I_{off} are collected while blocking the photoexcitation pulse before the sample. We sum the electron count over all the

pixels to compute the total electron flux. Fig. 2a) shows the fluctuation of the normalized scattered electron flux for a single image, $\sum_{\text{px}} I_{\text{on}}$, and for the shot-to-shot acquisition, $\sum_{\text{px}} I_{\text{on}}/\sum_{\text{px}} I_{\text{off}}$. We see that the fluctuation amplitude decreased by more than one order of magnitude with the shot-to-shot acquisition than the conventional method.

Fig. 2b) shows the frequency spectrum of the normalized signal. The relatively flat spectrum suggests that the noise is essentially composed of white noise in both acquisition modes. The shot-to-shot acquisition reduces the noise level at every time regime by a factor of 40 in low frequency and 30 in high frequency.

To quantitatively define the different noise origins, we write the overall noise level as³¹:

$$\sigma = \sqrt{\sigma_{\text{shot}}^2 + \sigma_{\text{source}}^2 + \sigma_{\text{white}}^2 + \sigma_{\text{readout}}^2 + \sigma_{\text{int}}^2 + \sigma_{\text{gain}}^2}, \quad (1)$$

where $\sigma_{\text{shot}} = \sqrt{n}$, with n the number of acquired electrons, is the intrinsic shot noise arising from the Poisson-distributed electron beam.

The source noise originates from fluctuations in the electron generation and the laser source which scales as $\sigma_{\text{source}} = \alpha_s \sqrt{f} \sqrt{N}$, with the electron flux f and the RMS magnitude α_s .

The white noise corresponds to the jitter and thermal effect of the optical and electron pulse generation scaling as $\sigma_{\text{white}} = \alpha_w N$.

The detector noise level defined as σ_{readout} and σ_{int} depends on the number of counts acquired at instantaneous and different integration times respectively when the electron beam is absent. The single electron detector doesn't have thermal noise like the CCD detector, then $\sigma_{\text{readout}} = 0$. This feature is crucial for utilizing the shot-to-shot acquisition method, as it prevents noise accumulation in each acquisition window. The main source of the integration noise σ_{int} is the cosmic rays detected by the Quadro. However, as shown in Fig. 2c), the flux of cosmic rays of 3.1 events/sec is insignificant compared to the electron flux usually set to $\sim 10^6$ electrons/sec. As described in Sec. II C, in the shot-to-shot mode, the exposure window is $25 \mu\text{s}$ so over one second the effective exposure time of the detector is 0.5 sec, reducing by a factor of two the integration noise level. The gain noise, σ_{gain} , originates from converting a collision event in the silicon detector to a written bit. As explained in Appendix A, this noise is negligible as long as we don't reach a saturation point of 1 electron/pixel/pulse.

The noise level is reduced to

$$\sigma = \sqrt{(\alpha \sqrt{N})^2 + (\alpha_w N)^2}, \quad (2)$$

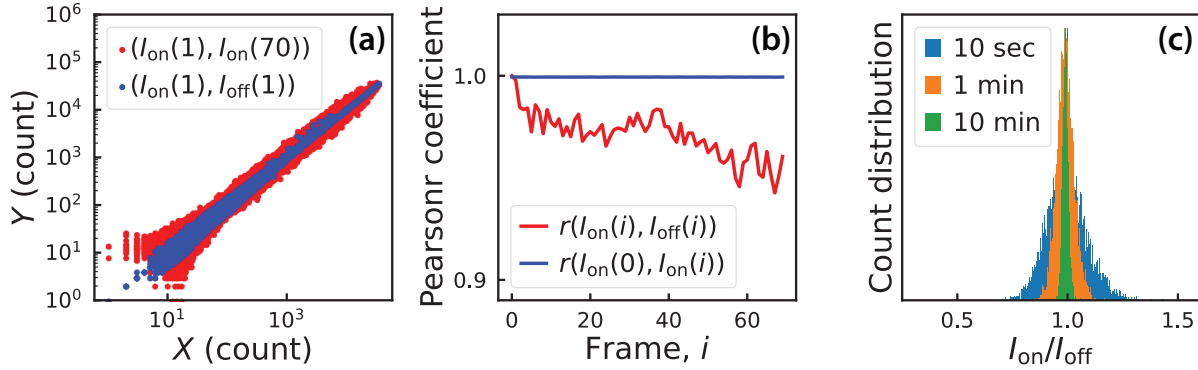


FIG. 3. a) Correlation between pixel values for the two modes of acquisition and b) the Pearson coefficient along frame time. c) Pixel values distribution of $I_{\text{on}}/I_{\text{off}}$ as function of the integration time.

with $\alpha = (1 + \alpha_s \sqrt{f})$. Fig. 2d) shows the noise level as a function of acquired electrons for single images and shot-to-shot mode for a flux of $f = 3.6 \cdot 10^6$ electrons/sec. It shows a source noise of $\alpha_s = 10^{-2} \text{ Hz}^{-1/2}$ and a white noise of $\alpha_w = 1.7 \cdot 10^{-2}$ for the single image whereas the shot-to-shot acquisition mode noise level reaches the shot noise with a source noise of $\alpha_s = 1.6 \cdot 10^{-4} \text{ Hz}^{-1/2}$ and a white noise, $\alpha_w = 1.5 \cdot 10^{-16}$, considered negligible.

Overall, Fig. 2 shows that the shot-to-shot mode decreases the noise level by almost a factor of 20. However, it requires twice the integration to build the reference image, so for twice the amount of signal, the SNR still increases by an order of magnitude.

B. Noise level with pump

In the presence of the pump, other noise sources from the thermal and mechanical fluctuation of the thin film should be considered. To verify how it affects real measurement, we focus our treatment on a pump-probe experiment before the temporal overlap between the pump and the probe, i.e. before t_0 . The reversible signal after the photo-excitation won't interfere with our treatment, but only the long-lived thermal and mechanical fluctuations.

We take a 50 nm thick sample of natural graphite as a studied specimen whose diffraction patterns are shown in Fig. 6c). We photoexcite the sample with an energy density of 0.8 mJ/cm^2 at a wavelength around 800 nm. Similar experiments have been reported with ultrafast electron diffraction^{2,3,10}, but in this section, we analyze the signal before the arrival time of the photoex-

citation pulse, which should correspond to the diffraction patterns without photoexcitation in the case of a reversible photoexcitation.

We analyze a set of $I_{\text{on}}^{(i)}$ and $I_{\text{off}}^{(j)}$ images corresponding to a ten-second exposure of graphite's diffraction patterns when it is photoexcited for a time window i , and when it is at rest for a time window j , respectively. For each diffraction image, we used a mask to set the unscattered electron beam to zero such that we compare only the fluctuation of the scattered electron. Despite a protection coating on the detector, the pump beam scattered in the chamber creates abnormal high-intensity pixels that are only visible on the I_{on} images. To remove them, we compare each image $I_{\text{on}}^{(i)}$ to $I_{\text{off}}^{(i)}$. The pixels on $I_{\text{on}}^{(i)}$ respecting the conditions $I_{\text{on}}^{(i)}/I_{\text{off}}^{(i)} > n$ and $I_{\text{on}}^{(i)}/I_{\text{off}}^{(i)} < 1/n$ are set to their $I_{\text{off}}^{(i)}$ value. For a cutting parameter $n = 2$, around 1.8% of the pixels are neutralized.

Fig. 3a) shows the correlation between $I_{\text{on}}^{(i)}$ and $I_{\text{off}}^{(i)}$ taken shot-to-shot, and between two diffraction patterns $I_{\text{on}}^{(i)}$ and $I_{\text{on}}^{(j)}$ taken few seconds apart, i.e. $i \neq j$. The pulse-to-pulse images are strongly correlated compared to the two single images, especially at low electron count pixel. We can characterize the correlation between the two images with the Pearson coefficient:

$$r(I_1, I_2) = \frac{\sum_x (I_1(x) - \langle I_1 \rangle)(I_2(x) - \langle I_2 \rangle)}{\sqrt{\sum_x (I_1(x) - \langle I_1 \rangle)^2 (I_2(x) - \langle I_2 \rangle)^2}}, \quad (3)$$

where the sum is over all the pixel x and $\langle I \rangle$ corresponds to the mean over the pixels. Fig 3b) shows the Pearson coefficient for a set of integrated images taken at different times. The correlation between $I_{\text{on}}^{(i)}$ and $I_{\text{off}}^{(i)}$ images taken shot-to-shot stays close to 1 while the one between $I_{\text{on}}^{(0)}$ and $I_{\text{on}}^{(j)}$ decreases and fluctuates with the time span between exposure. The average correlation between $\langle I_{\text{on}}(i), I_{\text{off}}(i) \rangle_i$ is $6.8 \cdot 10^{-4}$ close to 1 with a standard deviation of $1.6 \cdot 10^{-5}$. It suggests that the shot-to-shot acquisition mode is resilient to thermal and mechanical fluctuation, and these fluctuations stay stable.

Fig 3c) shows the pixel distribution of the normalization $I_{\text{on}}/I_{\text{off}}$ as a function of exposure time. We observe that it converges towards a Gaussian distribution with decreasing variance reaching 0.01 with a mean of 0.99. It confirms the robustness of the correlation between the diffraction pattern of the unpumped and pumped graphite.

C. Time resolution

One of the most important features of a UED setup is the time duration of the electron pulse at the sample position which defines the temporal resolution of the experiment³². The space charge

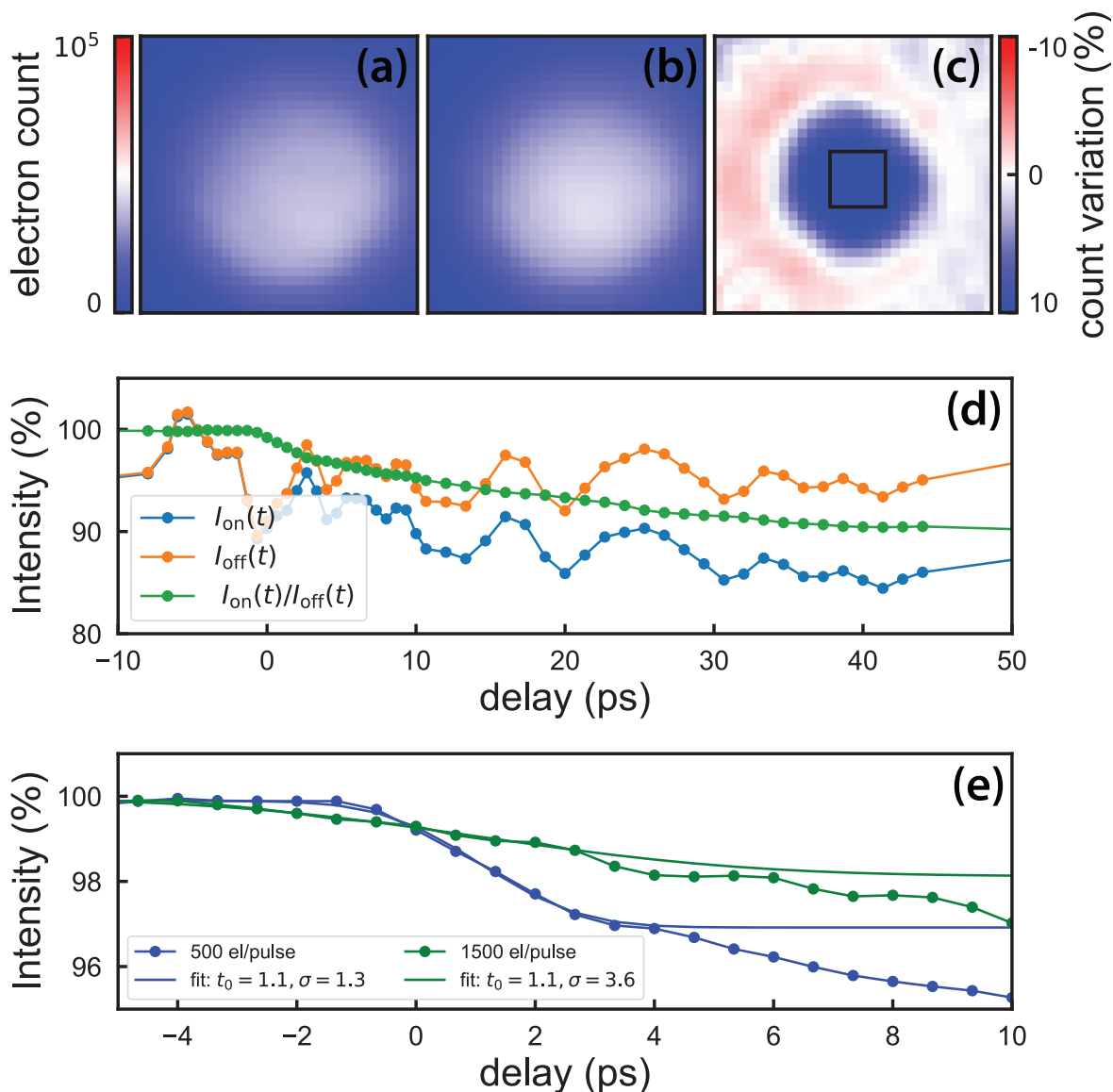


FIG. 4. Transient signal due to plasma generation after photoexcitation on a copper grid. Zoom in the unfocused electron beam that went through the copper grid after the photoexcitation photon pulse in a) the presence of the pump I_{on} , b) the absence of the pump I_{off} , and c) the normalization between each other I_{on}/I_{off} . d) Comparison between the transient signals measured for a region of interest in the center of the electron beam $I_{on}(t)$, $I_{off}(t)$, and $I_{on}(t)/I_{off}(t)$. e) Comparison of the normalized shot-to-shot transient signal of the plasma generation on the copper grid for different electron fluxes fitted with equation 4.

effect broadening the electron pulse in time and space is the limiting factor of the time resolution. To limit the space charge effect without a temporal compression scheme such as RF cavity or THz field^{17,18}, we place the electron source as close to the sample position as mechanically possible - around 15 cm.

We characterize the pulse duration to some extent with the convolution of step-function plasma generation $\Psi(t)$ on a copper grid and the electron pulse Gaussian distribution $g(t)$:

$$f(t) = \Psi(t) \star g(t) = A \cdot \text{Erfc} \left(\frac{t - t_0}{\sqrt{2}\sigma} \right), \quad (4)$$

with t_0 the time when the pump and the probe overlap on the sample, and A the signal amplitude. The parameter σ , corresponding to the variance of the Gaussian electron distribution, defines the temporal resolution of the experiment at a given electron flux.

We use a 1000 mesh copper grid and photoexcite at a wavelength of 800 nm with a fluence of 2 mJ/cm². Fig. 4a) and b) show the unfocused electron beam that went through the copper grid in the absence, $I_{\text{on}}(t)$, and the presence, $I_{\text{off}}(t)$, of the pump respectively at time t after the photoexcitation. Thanks to the shot-to-shot acquisition detection, the normalization between Fig. 4a) and b), $I_{\text{on}}/I_{\text{off}}$, shown in Fig. 4c), clearly reveals the pattern of the plasma after the photoexcitation. Fig. 4d) shows the total count in a region of interest defined as a 6×6 pixels highlighted by the square in Fig. 4c). Each delay corresponds to an exposure time $20 \cdot 10^3$ pulses for both $I_{\text{on}}(t)$, and $I_{\text{off}}(t)$. No transient signal can be observed for the single image acquisition since the noise level of 10% overcomes the physical signal of 5%. However, the normalization $I_{\text{on}}(t)/I_{\text{off}}(t)$ for each delay t increases the SNR by almost two orders of magnitude which reveals the physical transient signal due to the deflection of the electrons by the plasma generated after the photoexcitation.

When varying the flux of the electron, by varying the UV power, different transient dynamics are measured as shown in Fig. 4e). The transient signals are fitted with equation 4 to extract the temporal width of the electron beam σ . The temporal resolution gradually decreases as the electron flux increases.

The experimental results are compared to the mean-field calculation of the pulse length l through the second-order differential equation¹⁴:

$$\frac{d^2l}{dt} = \frac{Ne^2}{m_e \epsilon_0 \pi r^2} \left(1 - \frac{l}{\sqrt{l^2 + 4r^2}} \right). \quad (5)$$

With N , the number of electrons per bunch, e and m_e the electron charge and mass respectively, ϵ_0 the vacuum permittivity, and r the electron beam size.

The electron pulse duration is defined by $\Delta t = lv$, with the electron pulse velocity depending on the electron acceleration U through :

$$v = \sqrt{\frac{2eU}{m_e}}. \quad (6)$$

To work with the optimized configuration, we study the simulated temporal resolution depending on parameters that can be adjusted in the lab. Firstly, Fig. 5a) shows the electron pulse duration along the bunch's propagation distance for different electron fluxes from the numerical solution of Eq. 5. It suggests that the optimum distance to place the sample from the electron source is around 15 cm to keep the temporal resolution below 1 ps with a decent flux of a few thousand electrons per pulse.

Then, Fig. 5b) shows the small variation of the pulse duration as a function of the initial pulse duration, going from 1 fs to 1 ps. On the other hand, the pulse duration at 15 cm away from the electron source increases significantly when reducing the electron energy, mainly due to the longer time it takes for the electron to reach the sample's position. We extract that a few tens of keV electron energy is sufficient to keep the temporal resolution below 1 ps, while the initial pulse duration is not a sensitive parameter.

Lastly, Fig. 5c) shows the increase of temporal broadening with the decrease of the electron beam size. The broadening becomes significant for a beam size of around $500 \mu\text{m}$. As opposed to the Transmission Electron Microscope (TEM), the electron beam is focused on the electron detector to probe the sample's reciprocal space. Thus, the electron beam size is relatively large at the sample position in the UED setup - estimated at $400 \mu\text{m}$. After the sample, the electron beam size shrinks down to 100 nm without altering the temporal resolution. Fig. 5c) also displays the expected increase of the pulse duration as a function of the electron flux for a constant initial pulse duration of 100 fs. The time resolution is kept under 1 ps for flux lower than $5 \cdot 10^3$ electron/pulse and increases only slightly for low flux (under 500 electron/pulse). The experimental values extracted from the fit of Fig. 4e) are represented with the blue star markers. While the trend is consistent with the simulation, the temporal resolution is shifted by 1 ps. The simulation doesn't include the extreme space charge after the photo-emission when the electron bunch is accelerated in the cathode. In this region, a large Coulomb repulsion is expected within the dense electron bunch. However, we only expect a higher initial pulse duration which doesn't affect its dynamic after the electron source as shown in Fig. 5b).

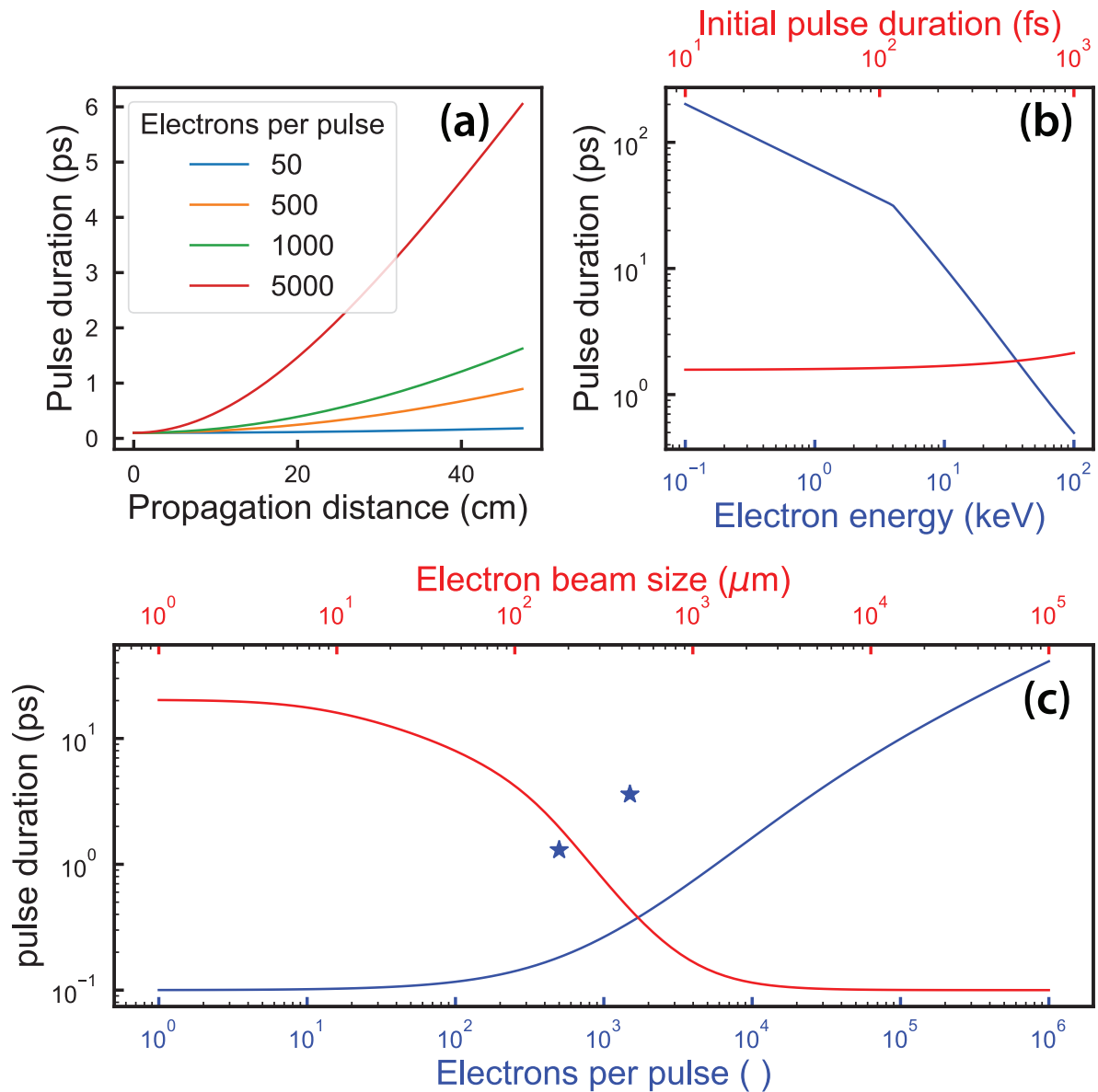


FIG. 5. a) Simulated pulse duration for different electron fluxes along the propagation distance for a $r = 200 \mu\text{m}$ accelerated at $U = 40 \text{ keV}$ with an initial pulse duration of 100 fs. b) Pulse duration at the sample's position (15 cm) as a function of the initial pulse duration t_0 (top axis), and electron energy U (bottom axis). c) Pulse duration at sample's position as a function of electron flux N , and electron beam size r . The experimental values are marked with blue stars for the pulse duration as a function of the number of electrons per pulse from Fig. 4e). For b) and c) the simulations are done by keeping $t_0 = 100 \text{ fs}$, $r = 200 \mu\text{m}$, $U = 40 \text{ keV}$, and $N = 10'000$ when not varying.

IV. REALISTIC SITUATION

The photo-induced plasma generation shows already a striking difference between the conventional and shot-to-shot acquisition methods. However, the intensity distribution with diffraction patterns relies on the sample geometry. Photo-induced thermal and mechanical effects can induce instability or artifacts. In Sec. III B we already showed that these effects are stable over time. In this section, we confirm the capabilities of the shot-to-shot acquisition method on a time-resolved experiment on Graphite.

Ultrafast electron diffraction experiment on Graphite has been already extensively studied^{2,10,17}. To account for the sensitivity of our acquisition techniques, we use a low absorbed excitation energy of 0.8 mJ/cm² on a 50 nm thick flake of natural graphite. The diffraction patterns are acquired over 24 hours, for an exposure of 22 min per delay (11 min for $I_{\text{on}}(t)$ and $I_{\text{off}}(t)$ respectively). To overcome the slight zone axis misalignment and gain SNR, we averaged the diffraction patterns along the 6-fold symmetry axis, as shown in Fig. 6c).

To observe the photo-induced effect we normalize the excited diffraction patterns by the one at rest and subtract this by the same ratio averaged along delays before time zero, t_0 , when the pump pulse arrives after the probe one. The subtraction removes the constant thermal effect. It can be written as:

$$\Delta I(t, \mathbf{q}) = \frac{I_{\text{on}}(t, \mathbf{q})}{I_{\text{off}}(t, \mathbf{q})} - \frac{\langle I_{\text{on}}(t, \mathbf{q}) \rangle_{t < t_0}}{\langle I_{\text{off}}(t, \mathbf{q}) \rangle_{t < t_0}} \quad (7)$$

This normalization is shown in Fig. 6a) at a time delay $t = 1$ ps after the photoexcitation. Since the normalization occurs pixel by pixel, the noise increases significantly in low-intensity regions. This effect is visible on the side of the figure where the signal is the lowest. To avoid this effect, we can subtract the pumped diffraction pattern from the unpumped as:

$$\delta I(t, \mathbf{q}) = \frac{I_{\text{on}}(t, \mathbf{q})}{\langle I_{\text{on}}(t, \mathbf{q}) \rangle_{\mathbf{q}}} - \frac{I_{\text{off}}(t, \mathbf{q})}{\langle I_{\text{off}}(t, \mathbf{q}) \rangle_{\mathbf{q}}} - \left\langle \frac{I_{\text{on}}(t, \mathbf{q})}{\langle I_{\text{on}}(t, \mathbf{q}) \rangle_{\mathbf{q}}} - \frac{I_{\text{off}}(t, \mathbf{q})}{\langle I_{\text{off}}(t, \mathbf{q}) \rangle_{\mathbf{q}}} \right\rangle_{t < t_0} \quad (8)$$

Fig. 6c) shows this subtraction for a time delay $t = 1$ ps. In this case, there is a strong signature where the electron intensity is large, at the Bragg peak position, but we can still resolve the low variation in the diffuse scattering at the K-point.

The transient dynamics account for the sensitivity of the setup qualitatively. Fig. 6d) shows the intensity variation for the 100 Bragg peak family and the diffuse scattering at the K -point and around the Γ_{110} Bragg peak highlighted in the diffraction pattern Fig 6c). The low excitation energy induces a diffraction decrease of only 0.1% due to the Debye-Waller effect. We can still

resolve the transition between the fast initial drop from the generation of strongly coupled optical (SCOP) phonon to the slower one from their decay to acoustic phonon at 1 ps. This is consistent with the fast increase of the diffuse scattering intensity at the K-point due to the generation of A'_1 optical phonon. Its population starts decreasing at 2 ps as it scatters with lower energy near Γ momentum acoustic phonons as suggested by the transient dynamics of diffuse scattering around the Γ_{110} Bragg peak family. These results are consistent with the previous work of Stern *et al*¹⁰ in which the photoexcitation energy is 15 times higher than the one used here.

V. CONCLUSION

Similar to ultrafast optical spectroscopy, the shot-to-shot acquisition method improves significantly the signal-to-noise ratio for the study of transient dynamics in solids and molecules. By phase locking a high acquisition rate direct electron detector, the noise reaches the shot noise limit. By introducing a photoexcitation pulse, we observe thermal and mechanical fluctuations that are stable over time and don't introduce additional white noise. The signal can be improved by increasing the electron flux with the only limitations being the temporal resolution and the detection saturation. The first can be overcome with temporal compression while the latter is lifted in the low scattering region.

The simulation of the temporal broadening indicates the right balance between electron flux and temporal resolution. The high sensitivity allows the investigation of ultrafast lattice dynamics after a low photo-excitation perturbation. It avoids thermal effects that can interfere with coherent effects or initiate phase transition.

Shot-to-shot acquisition schemes can be implemented in other electronic spectroscopy methods such as ultrafast Lorentz TEM, time-resolved electron energy loss spectroscopy (tr-EELS), time and angle-resolved photoemission spectroscopy (tr-ARPES), and others. It paves the way for the investigation of sensitive materials in the low perturbation regime.

Appendix A: Quantum detection efficiency

When an electron collides with a detector's pixel, charges are displaced and a signal is acquired. If it reaches a given threshold, the detector counts one electron. The threshold is factory-calibrated

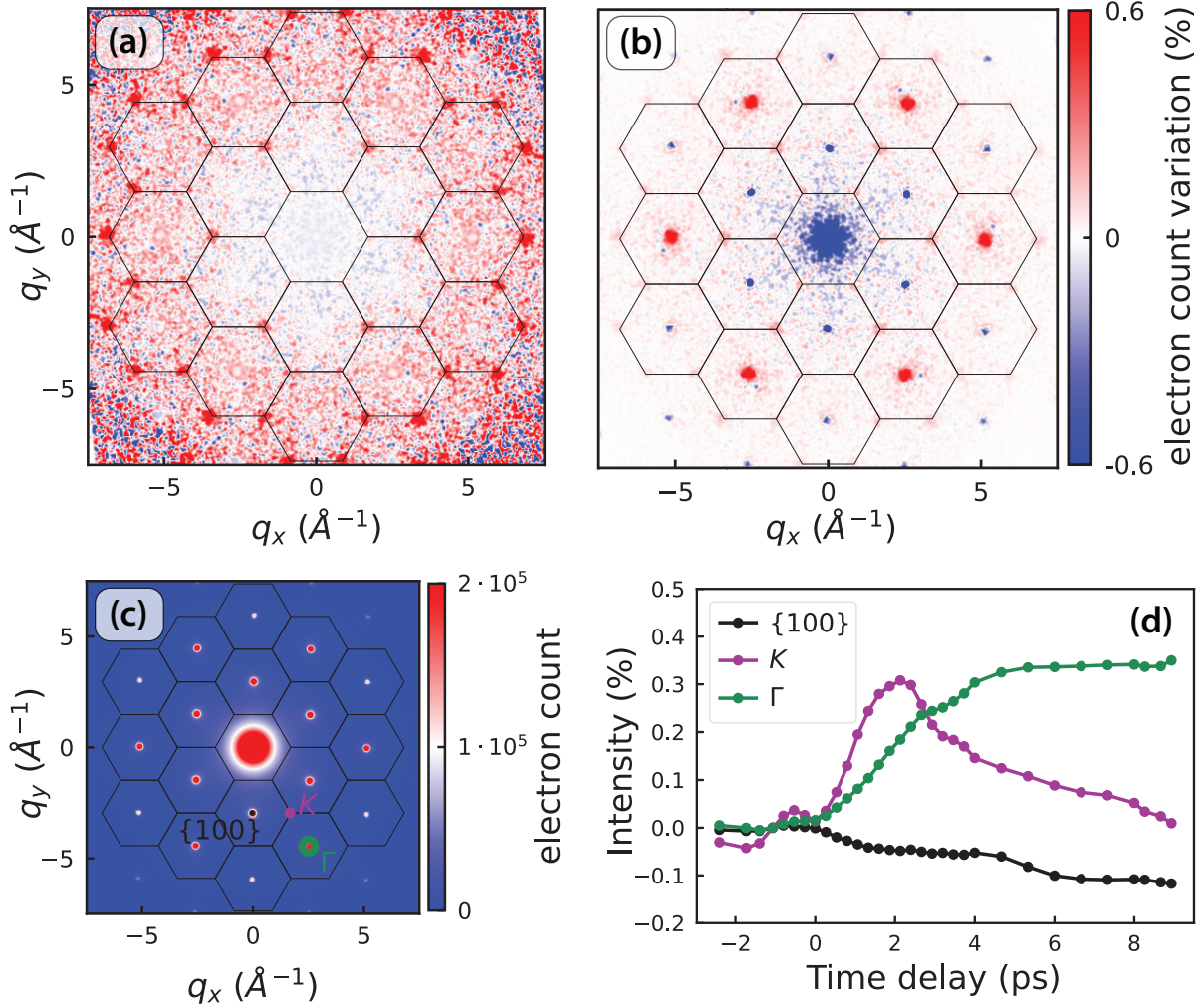


FIG. 6. a) and b) are the normalized diffraction patterns as equation 7 and 8 respectively, averaged over a time delay, t , between 1 and 2 ps. c) 6-fold averaged diffraction patterns of Graphite, corresponding to $I_{\text{on}}(t = -2.4 \text{ ps}, \mathbf{q})$. d) Electron count variation for specific regions of interest highlighted in panel c) corresponding to the Bragg peak family 100 and the diffuse scattering at reduced momentum K and around the Γ point.

for different electron energies.

By measuring the electron flux for different UV power, we can study the quantum detection efficiency defined as

$$QDE = \frac{n_{\text{el}}}{n_{\text{ph}}}, \quad (\text{A1})$$

where n_{el} is the number of acquired electrons per pulse directly measured by the direct electron detector for one second exposure time. $n_{\text{ph}} = P/fE_{\text{ph}}$ is the number of photons per pulse for a repetition rate $f = 20 \text{ kHz}$, a photon energy $E_{\text{ph}} = 4.66 \text{ eV}$ and beam power P measured with a

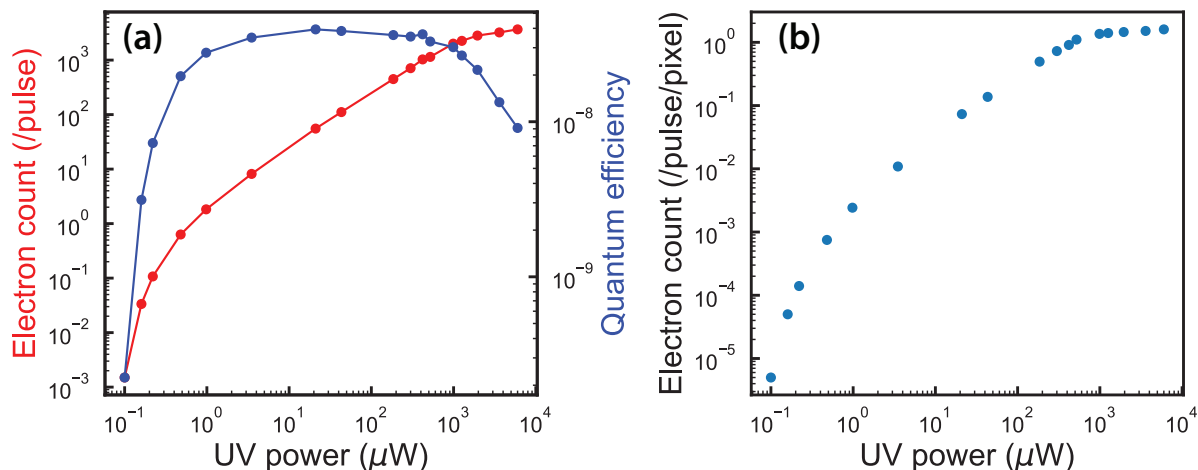


FIG. 7. (a) Electron flux and quantum detection efficiency (Eq. A1) as a function of the input UV power for an electron energy of 30 keV. (b) Acquired electron per pulse for one selected pixel as a function of the UV power.

power meter.

Fig. 7a) shows the acquired electron, n_{el} and the quantum detection efficiency, QDE , as a function of the input UV power. The latter reveals a plateau from $1 \mu\text{W}$ and decreases $10^3 \mu\text{W}$ when the flux reaches 10^3 electrons/pulse.

The flux saturation can be due to the space charge and thermal effect of the photocathode. Another more probable explanation is the detection saturation. The detector counts one electron for a given pixel when its signal reaches a threshold. When the signal is higher than the threshold for longer than 200 ns, the detector counts another electron. This retrigger unit enables high electron flux measurement for continuous beam, but for a short pulsed beam of time duration $\ll 200$ ns, the electron bunch is dense enough so that the detector cannot acquire more than one electron per pixel per pulse. Fig. 7b) illustrates this by showing the electron count for one pixel as a function of the input UV power. From one electron/pulse/pixel, the acquired count starts saturating. It is not favored to use a high pulsed electron flux with this kind of direct electron detector, as artifacts can arise from the detection saturation.

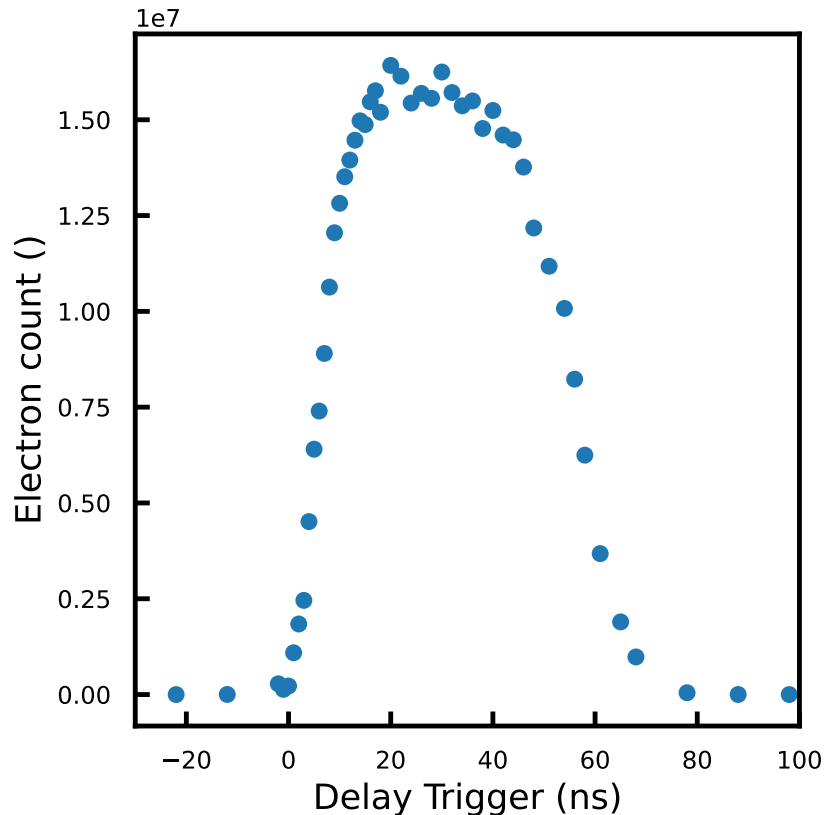


FIG. 8. Electron count measured by the Quadro as a function of the delay given to a square signal with fixed width.

Appendix B: Electronic response of the detector to an electron pulse

Electron detectors can have a long recovery time after an electron bunch arrival. If the recovery time is longer than the delay between two pulses, the shot-to-shot acquisition can lose its benefits. To quantify the electronic response of the direct electron detector we vary the delay of the acquisition window from the laser trigger with a fixed width of 10 ns. The delay can be tuned with steps down to 1 ns. For each delay, we acquire an image of the raw electron beam with one-second exposure in shot-to-shot acquisition mode. Fig. 8 shows the total electron count as a function of the trigger delay. Even though the electron pulse duration is around 1 ps, the signal acquired by the detector lasts 80 ns. Then, the recovery time is smaller than the one between the pulse ($50\mu\text{s}$).

REFERENCES

- ¹A. H. Zewail, “Four-dimensional electron microscopy,” *Science* **328**, 187–193 (2010), <https://www.science.org/doi/pdf/10.1126/science.1166135>.
- ²F. Carbone, P. Baum, P. Rudolf, and A. H. Zewail, “Structural preablation dynamics of graphite observed by ultrafast electron crystallography,” *Physical Review Letters* **100**, 035501 (2008), publisher: American Physical Society.
- ³R. P. Chatelain, V. R. Morrison, B. L. M. Klarenaar, and B. J. Siwick, “Coherent and incoherent electron-phonon coupling in graphite observed with radio-frequency compressed ultrafast electron diffraction,” *Phys. Rev. Lett.* **113**, 235502 (2014).
- ⁴N. Rubiano da Silva, M. Möller, A. Feist, H. Ulrichs, C. Ropers, and S. Schäfer, “Nanoscale mapping of ultrafast magnetization dynamics with femtosecond lorentz microscopy,” *Phys. Rev. X* **8**, 031052 (2018).
- ⁵G. Berruto, I. Madan, Y. Murooka, G. Vanacore, E. Pomarico, J. Rajeswari, R. Lamb, P. Huang, A. Kruchkov, Y. Togawa, T. LaGrange, D. McGrouther, H. Rønnow, and F. Carbone, “Laser-Induced Skyrmion Writing and Erasing in an Ultrafast Cryo-Lorentz Transmission Electron Microscope,” *Physical Review Letters* **120**, 117201 (2018), publisher: American Physical Society.
- ⁶N. Rubiano da Silva, M. Möller, A. Feist, H. Ulrichs, C. Ropers, and S. Schäfer, “Nanoscale Mapping of Ultrafast Magnetization Dynamics with Femtosecond Lorentz Microscopy,” *Physical Review X* **8**, 031052 (2018), publisher: American Physical Society.
- ⁷L. Piazza, T. T. A. Lummen, E. Quiñonez, Y. Murooka, B. W. Reed, B. Barwick, and F. Carbone, “Simultaneous observation of the quantization and the interference pattern of a plasmonic near-field,” *Nature Communications* **6**, 6407 (2015), publisher: Nature Publishing Group.
- ⁸Y. Cheng, A. Zong, L. Wu, Q. Meng, W. Xia, F. Qi, P. Zhu, X. Zou, T. Jiang, Y. Guo, J. Van Wezel, A. Kogar, M. W. Zuerch, J. Zhang, Y. Zhu, and D. Xiang, “Ultrafast formation of topological defects in a two-dimensional charge density wave,” *Nature Physics* **20**, 54–60 (2024).
- ⁹L. P. René De Cotret, J.-H. Pöhls, M. J. Stern, M. R. Otto, M. Sutton, and B. J. Siwick, “Time- and momentum-resolved phonon population dynamics with ultrafast electron diffuse scattering,” *Phys. Rev. B* **100**, 214115 (2019).
- ¹⁰M. J. Stern, L. P. René de Cotret, M. R. Otto, R. P. Chatelain, J.-P. Boisvert, M. Sutton, and B. J. Siwick, “Mapping momentum-dependent electron-phonon coupling and nonequilibrium phonon

- dynamics with ultrafast electron diffuse scattering,” *Phys. Rev. B* **97**, 165416 (2018), publisher: American Physical Society.
- ¹¹L. Waldecker, R. Bertoni, H. Hübener, T. Brumme, T. Vasileiadis, D. Zahn, A. Rubio, and R. Ernstorfer, “Momentum-Resolved View of Electron-Phonon Coupling in Multilayer $\{\mathrm{WSe}\}_2$,” *Physical Review Letters* **119**, 036803 (2017), publisher: American Physical Society.
- ¹²R. M. van der Veen, T. J. Penfold, and A. H. Zewail, “Ultrafast core-loss spectroscopy in four-dimensional electron microscopy,” **2**, 024302.
- ¹³K. Lyon, A. Bergman, P. Zeiger, D. Kepaptsoglou, Q. M. Ramasse, J. C. Idrobo, and J. Rusz, “Theory of magnon diffuse scattering in scanning transmission electron microscopy,” *Physical Review B* **104**, 214418 (2021), publisher: American Physical Society.
- ¹⁴B. J. Siwick, J. R. Dwyer, R. E. Jordan, and R. J. D. Miller, “Ultrafast electron optics: Propagation dynamics of femtosecond electron packets,” *Journal of Applied Physics* **92**, 1643–1648 (2002).
- ¹⁵X. Wang, S. Nie, H. Park, J. Li, R. Clinite, R. Li, X. Wang, and J. Cao, “Measurement of femtosecond electron pulse length and the temporal broadening due to space charge,” *Review of Scientific Instruments* **80**, 013902 (2009).
- ¹⁶G. F. Mancini, B. Mansart, S. Pagano, B. van der Geer, M. de Loos, and F. Carbone, “Design and implementation of a flexible beamline for fs electron diffraction experiments,” *Nuclear Instruments and Methods in Physics Research Section A: Accelerators, Spectrometers, Detectors and Associated Equipment* **691**, 113–122 (2012).
- ¹⁷R. P. Chatelain, V. R. Morrison, C. Godbout, and B. J. Siwick, “Ultrafast electron diffraction with radio-frequency compressed electron pulses,” *Applied Physics Letters* **101**, 081901 (2012).
- ¹⁸D. Ehberger, K. J. Mohler, T. Vasileiadis, R. Ernstorfer, L. Waldecker, and P. Baum, “Terahertz Compression of Electron Pulses at a Planar Mirror Membrane,” *Physical Review Applied* **11**, 024034 (2019), publisher: American Physical Society.
- ¹⁹M. R. Otto, L. P. René de Cotret, M. J. Stern, and B. J. Siwick, “Solving the jitter problem in microwave compressed ultrafast electron diffraction instruments: Robust sub-50 fs cavity-laser phase stabilization,” *Structural Dynamics* **4**, 051101 (2017).
- ²⁰L. Waldecker, R. Bertoni, and R. Ernstorfer, “Compact femtosecond electron diffractometer with 100 keV electron bunches approaching the single-electron pulse duration limit,” *Journal of Applied Physics* **117**, 044903 (2015).

- ²¹B. Freelon, T. Rohwer, A. Zong, A. Kogar, H. Zhou, L. J. Wong, E. Ergeçen, and N. Gedik, “Design and construction of a compact, high-repetition-rate ultrafast electron diffraction instrument,” *Review of Scientific Instruments* **94**, 053305 (2023).
- ²²M. Aidelsburger, F. O. Kirchner, F. Krausz, and P. Baum, “Single-electron pulses for ultrafast diffraction,” *Proceedings of the National Academy of Sciences* **107**, 19714–19719 (2010), publisher: Proceedings of the National Academy of Sciences.
- ²³Quadro, Dectris.
- ²⁴G. McMullan, A. R. Faruqi, and R. Henderson, “Chapter One - Direct Electron Detectors,” in *Methods in Enzymology*, The Resolution Revolution: Recent Advances In cryoEM, Vol. 579, edited by R. A. Crowther (Academic Press, 2016) pp. 1–17.
- ²⁵B. D. A. Levin, “Direct detectors and their applications in electron microscopy for materials science,” *Journal of Physics: Materials* **4**, 042005 (2021), publisher: IOP Publishing.
- ²⁶C. J. R. Duncan, M. Kaemingk, W. H. Li, M. B. Andorf, A. C. Bartnik, A. Galdi, M. Gordon, C. A. Pennington, I. V. Bazarov, H. J. Zeng, F. Liu, D. Luo, A. Sood, A. M. Lindenberg, M. W. Tate, D. A. Muller, J. Thom-Levy, S. M. Gruner, and J. M. Maxson, “Multi-scale time-resolved electron diffraction: A case study in moiré materials,” *Ultramicroscopy* **253**, 113771 (2023).
- ²⁷B. Lang, “Photometrics of ultrafast and fast broadband electronic transient absorption spectroscopy: State of the art,” *Review of Scientific Instruments* **89**, 093112 (2018).
- ²⁸Wyvern, KM Labs.
- ²⁹F. Pennacchio, G. M. Vanacore, G. F. Mancini, M. Oppermann, R. Jayaraman, P. Musumeci, P. Baum, and F. Carbone, “Design and implementation of an optimal laser pulse front tilting scheme for ultrafast electron diffraction in reflection geometry with high temporal resolution,” *Structural Dynamics* **4**, 044032 (2017).
- ³⁰GlazPD, Synertronic design.
- ³¹C. Kealhofer, S. Lahme, T. Urban, and P. Baum, “Signal-to-noise in femtosecond electron diffraction,” *Ultramicroscopy* **159**, 19–25 (2015).
- ³²M. T. Hassan, J. S. Baskin, B. Liao, and A. H. Zewail, “High-temporal-resolution electron microscopy for imaging ultrafast electron dynamics,” *Nature Photonics* **11**, 425–430 (2017), publisher: Nature Publishing Group.
- ³³C. Giannetti, G. Coslovich, F. Cilento, G. Ferrini, H. Eisaki, N. Kaneko, M. Greven, and F. Parmigiani, “Discontinuity of the ultrafast electronic response of underdoped superconducting $\text{Bi}_2\text{Sr}_2\text{CaCu}_2\text{O}_{8+\delta}$ strongly excited by ultrashort light pulses,” *Physical Review B* **79**, 224502

Shot-to-shot acquisition ultrafast electron diffraction

(2009), publisher: American Physical Society.